

# Estimation of uncertainties in the density driven flow in fractured porous media using MLMC

Dmitry Logashenko<sup>1</sup>, Alexander Litvinenko<sup>2\*</sup>, Raul Tempone<sup>1,2</sup>,  
Gabriel Wittum<sup>1</sup>

<sup>1</sup>\*CSE Department, KAUST, Thuwal-Jeddah, Saudi Arabia.

<sup>2</sup>Department of Mathematics, RWTH Aachen, Aachen, Germany.

\*Corresponding author(s). E-mail(s): [litvinenko@uq.rwth-aachen.de](mailto:litvinenko@uq.rwth-aachen.de);

Contributing authors: [dmitry.logashenko@kaust.edu.sa](mailto:dmitry.logashenko@kaust.edu.sa);

[raul.tempone@kaust.edu.sa](mailto:raul.tempone@kaust.edu.sa); [gabriel.wittum@kaust.edu.sa](mailto:gabriel.wittum@kaust.edu.sa);

## Abstract

We use the Multi Level Monte Carlo method to estimate uncertainties in a Henry-like salt water intrusion problem with a fracture. The flow is induced by the variation of the density of the fluid phase, which depends on the mass fraction of salt. We assume that the fracture has a known fixed location but an uncertain aperture. Other input uncertainties are the porosity and permeability fields and the recharge. In our setting, porosity and permeability vary spatially and recharge is time-dependent. For each realisation of these uncertain parameters, the evolution of the mass fraction and pressure fields is modelled by a system of non-linear and time-dependent PDEs with a jump of the solution at the fracture. The uncertainties propagate into the distribution of the salt concentration, which is an important characteristic of the quality of water resources. We show that the multilevel Monte Carlo (MLMC) method is able to reduce the overall computational cost compared to classical Monte Carlo methods. This is achieved by balancing discretisation and statistical errors. Multiple scenarios are evaluated at different spatial and temporal mesh levels. The deterministic solver `ug4` is run in parallel to calculate all stochastic scenarios.

**Keywords:** uncertainty quantification, MLMC, density-driven flow, aquifer, porosity, permeability, fracture, multigrid methods

# Contents

<b>1</b>	<b>Introduction</b>	<b>2</b>
<b>2</b>	<b>Modeling and Problem Settings</b>	<b>4</b>
2.1	Governing equations for the flow . . . . .	4
2.2	Model problem settings . . . . .	6
2.3	Stochastic modeling of porosity, permeability and fracture width . . . .	8
<b>3</b>	<b>Numerical Methods</b>	<b>9</b>
3.1	Numerical methods for the deterministic problem . . . . .	9
3.2	MLMC Algorithm . . . . .	10
<b>4</b>	<b>Numerical Experiments</b>	<b>14</b>
4.1	The mean value and variance . . . . .	16
4.2	Estimation of convergence rates $\alpha$ and $\beta$ for various QoIs . . . . .	17
4.3	Comparison of MC and MLMC methods . . . . .	18
<b>5</b>	<b>Discussion and Conclusion</b>	<b>19</b>

## 1 Introduction

An important and challenging problem in hydrogeology is the modeling of density-driven subsurface flow and salt transport in fractured aquifers. Essential difficulties in these settings are complicated and parameter-sensitive flow pattern due to the fractures as well as a number of the uncertain parameters. Uncertainties in the fracture geometry, porosity, permeability, recharge can strongly influence the evolution of the salt concentration in the subsurface (cf. [1, 3, 4, 33, 44]). In a real reservoir the number of the fractures, their location and their aperture are uncertain. One possible solution approach would be to model all these uncertainties, build a PCE-based surrogate, perform a sensitive analysis (see [5, 45]) to understand which uncertainties are very critical and which are not, and estimate how they contribute to the solution. This is a very non-trivial approach. Instead, we apply the Multi Level Monte Carlo method (MLMC) method. Another reason for the usage of MLMC method is that the deterministic problem is resolved via the multigrid method. So, there is a natural idea to try to couple the MLMC and multigrid methods.

An essential problem in water production from coastal aquifers is their salinization due to the intrusion of the seawater. Salt concentration in the drinking water should be kept below the prescribed limits, and therefore its forecast is important for water resources management in coastal regions.

Fractures introduce heterogeneity in the aquifer that affects fluid flow and makes it difficult to predict its main characteristics. A challenge is that fractures can get sealed over time, reducing their permeability and affecting fluid flow. In summary, adding fractures to subsurface aquifers presents challenges related to complexity, sealing, heterogeneity and environmental concerns. However, with careful planning and

management, fractures can also provide opportunities for increased production and improved reservoir performance.

As a model problem, we consider the benchmark from [20] which is a generalization of the Henry problem first introduced in [25]. The Henry problem became a benchmark for numerical solvers for the density-driven groundwater flow (see [14, 42, 43, 50]. In [39], the authors use the generalised polynomial chaos expansion approximation to investigate how incomplete knowledge of system properties affects the assessment of global quantities. In particular, they estimated the propagation of input uncertainties into a few dimensionless scalar parameters.

In [20, 21, 38], the authors modeled and computed the density-driven flow in fractured porous media with deterministic settings. The fractures considered were represented by a  $(d-1)$ -dimensional manifolds in a  $d$ -dimensional domain. They developed a special numerical technique based on the finite volume method and implemented it in the ug3 library. In our present work, we apply the same model, the same discretization and solvers to compute the multiple uncertain scenarios.

In [21], the validity of the low-dimensional representation of the fractures has been addressed. The authors considered both  $d$  and  $(d-1)$ -dimensional fractures. They have shown numerically that the  $(d-1)$ -dimensional representation can be a valid alternative to the full-dimensional resolution of all the subdomains provided that the fracture apertures are in some reasonable range. All the settings in this work were deterministic.

Other methods based on  $(d-1)$ -dimensional representation of fractures were considered in [1, 3, 4, 19, 33, 41, 44].

Many techniques can be used to quantify uncertainties. One classical method is Monte Carlo (MC) sampling. It has a well-known disadvantage — a slow convergence  $\mathcal{O}(\frac{1}{\sqrt{N}})$ . Other relative recent techniques such as surrogate models and stochastic collocation may require a few hundred time-consuming simulations and assume a certain smoothness of the quantity of interest (QoI).

Another class of methods is the class of perturbation methods [12]. The idea is to decompose the QoI with respect to random parameters in a Taylor series. The higher order terms can be neglected for small perturbations, simplifying the analysis and numerics. These methods assume that the random perturbations are small. For larger perturbations, these methods usually do not work.

There are a number of studies where authors have modeled uncertainties in reservoirs (see [7, 48]). The link between stochastic methods and hydrogeological applications was made in [6]. Further the authors made recommendations to water suppliers in Germany about optimisation and risk assessment. The basics of stochastic hydrogeology and an overview of stochastic tools and uncertainty management are described in [40].

The review [46] deals with hydrogeological applications of recent advances in uncertainty quantification, probabilistic risk assessment and decision making under uncertainty.

This work has the following structure. Section 2 describes the model. Section 3 contains description of numerical methods. In particular, the well-known MLMC method is reviewed in Section 3.2. Section 4 details the numerical results, which include the

numerical analysis of the model problem, the computation of different statistics, the performance of the MLMC method, and the performance of the parallel solver with uncertain coefficients. Finally, we conclude this work with a discussion in Section 5.

## 2 Modeling and Problem Settings

We consider the density driven flow of the liquid phase (salt solution in water) with variable mass fraction of the salt in a fractured aquifer. The fractures are geological formations whose size in one of the geometrical directions is negligible in comparison with the scales of the domain whereas the permeability of the filling material is much higher than that of the surrounding medium. This causes essential problems when these fractures are considered as full-dimensional subdomains in the simulations: Specific, very fine grids needed for the resolution of this sort of the objects as well as the strong jump of the model parameters reduces the efficiency of the numerical methods significantly. For this reason, several other approaches have been developed where the fractures are represented by low-dimensional manifolds and the fracture aperture (width) is a parameter (cf. [1, 4, 13, 16, 28, 32, 38]). Whereas it has been shown that for the density-driven flow, these models provide a proper approximation only for a certain range of the fracture width ([21]), their application is considered to be reasonable in many situations. A particular advantage of such the models for the sampling methods is the possibility to change the fracture width without remeshing of the entire domain. In this paper, we assume that the porous matrix is immobile and the fractures do not change their positions.

### 2.1 Governing equations for the flow

In this section, we briefly describe the PDEs and refer to [36, 38] for details. From the modeling point of view, we consider the porous medium  $\mathcal{M} \subset \mathcal{D}$  surrounding the fracture with the porosity  $\phi_m : \mathcal{M} \rightarrow (0, 1)$  and the permeability  $\mathbf{K}_m : \mathcal{M} \rightarrow \mathbb{R}^{d \times d}$ . The fluid phase in this subdomain is characterized by salt mass fraction  $c_m(t, \mathbf{x}) : [0, +\infty) \times \mathcal{M} \rightarrow [0, 1]$  and pressure  $p_m(t, \mathbf{x}) : [0, +\infty) \times \mathcal{M} \rightarrow \mathbb{R}$ . So, the flow in  $\mathcal{M}$  obeys the standard mass conservation laws for the entire liquid phase and the salt

$$\left. \begin{aligned} \partial_t(\phi_m \rho_m) + \nabla \cdot (\rho_m \mathbf{q}_m) &= 0 \\ \partial_t(\phi_m \rho_m c_m) + \nabla \cdot (\rho_m c_m \mathbf{q}_m - \rho_m \mathbf{D}_m \nabla c_m) &= 0 \end{aligned} \right\} \quad x \in \mathcal{M} \quad (1)$$

with the Darcy's law for the velocity:

$$\mathbf{q}_m = -\frac{\mathbf{K}_m}{\mu_m}(\nabla p_m - \rho_m \mathbf{g}), \quad x \in \mathcal{M}, \quad (2)$$

where  $\rho_m = \rho(c_m)$  and  $\mu_m = \mu(c_m)$  indicate the density and the viscosity of the liquid phase,  $\mathbf{D}_m(t, \mathbf{x}) : [0, +\infty) \times \mathcal{M} \rightarrow \mathbb{R}^{d \times d}$  denotes the molecular diffusion and mechanical dispersion tensor.

The fracture is assumed to be filled with a porous medium, too. In particular, we assume the validity of the Darcy's law inside the fracture. Without loss of generality,

we consider in this work only one fracture, see [36, 38] for the generalization. The fracture is represented by a surface  $\mathcal{S} \subset \mathcal{D}$ ,  $\mathcal{M} \cup \mathcal{S} = \mathcal{D}$ ,  $\mathcal{M} \cap \mathcal{S} = \emptyset$ . However, we distinguish between the two sides of the fracture,  $\mathcal{S}^{(1)}$  and  $\mathcal{S}^{(2)}$ , that geometrically coincide with  $\mathcal{S}$  but are virtually interfaces of the fracture with  $\mathcal{M}$  and have opposite normals  $\mathbf{n}^{(1)}$  and  $\mathbf{n}^{(2)}$ .

For the fluid phase inside the fracture, let  $c_f : [0, +\infty) \times \mathcal{S} \rightarrow [0, 1]$  and  $p_f : [0, +\infty) \times \mathcal{S} \rightarrow \mathbb{R}$  be the salt mass fraction and the pressure averaged along the vertical, cf. [21]. Note that in general, the values of  $c_f$  and  $p_f$  are not equal to the limits of  $c_m$  and  $p_m$  at  $\mathcal{S}$ . Furthermore, the latter limits may be different on  $\mathcal{S}^{(1)}$  and  $\mathcal{S}^{(2)}$ . We denote them by  $c_m^{(1)}$  and  $c_m^{(2)}$ , as well as  $p_m^{(1)}$  and  $p_m^{(2)}$  as functions on  $\mathcal{S}^{(1)}$  and  $\mathcal{S}^{(2)}$ , respectively. Two sets of the equations are stated for the fracture: The laws that describe the flow along the fracture and the ones modeling the mass exchange through the interfaces  $\mathcal{S}^{(1)}$  and  $\mathcal{S}^{(2)}$ .

For the lateral flow in the fracture, we impose the analogues of the mass conservation laws (1):

$$\left. \begin{aligned} \partial_t(\phi_f \epsilon \rho_f) + \nabla^{\mathcal{S}} \cdot (\epsilon \rho_f \mathbf{q}_f) + Q_{fn}^{(1)} + Q_{fn}^{(2)} &= 0 \\ \partial_t(\phi_f \epsilon \rho_f c_f) + \nabla^{\mathcal{S}} \cdot (\epsilon \rho_f c_f \mathbf{q}_f - \epsilon \rho_f D_f \nabla^{\mathcal{S}} c_f) + P_{fn}^{(1)} + P_{fn}^{(2)} &= 0 \end{aligned} \right\} \quad x \in \mathcal{S}, \quad (3)$$

where  $\nabla^{\mathcal{S}}$  denotes the differential operators on the manifold  $\mathcal{S}$  and  $\epsilon$  the fracture width. The Darcy velocity along the fracture is

$$\mathbf{q}_f = -\frac{K_f}{\mu_f} (\nabla^{\mathcal{S}} p_f - \rho_f \mathbf{g}), \quad x \in \mathcal{S}. \quad (4)$$

In (3-4),  $\rho_f = \rho(c_f)$  and  $\mu_f = \mu(c_f)$  are the density and the viscosity of the fluid phase in the fracture. Furthermore,  $\phi_f : \mathcal{S} \rightarrow [0, 1]$  denotes the porosity associated with the material in the fracture,  $K_f : \mathcal{S} \rightarrow \mathbb{R}$  its lateral permeability and  $D_f(t, x) : [0, +\infty) \times \mathcal{S} \rightarrow \mathbb{R}$  the lateral diffusion and dispersion tensor in the fracture.

The terms  $Q_{fn}^{(k)}$  and  $P_{fn}^{(k)}$ ,  $k \in \{1, 2\}$ , are the mass fluxes through the faces  $\mathcal{S}^{(k)}$  of the fracture, i.e. the normal fluxes. They are defined as

$$\left. \begin{aligned} Q_{fn}^{(k)} &:= \rho(c_m^{(k)}) q_{fn}^{(k)} \\ P_{fn}^{(k)} &:= \rho(c_m^{(k)}) c_{\text{upwind}}^{(k)} q_{fn}^{(k)} - \rho(c_m^{(k)}) D_{fn}^{(k)} \frac{c_m^{(k)} - c_f}{\epsilon/2} \end{aligned} \right\} \quad x \in \mathcal{S}^{(k)}, \quad (5)$$

where  $c_{\text{upwind}}^{(k)} = c_m^{(k)}$  if  $q_{fn}^{(k)} < 0$  but  $c_{\text{upwind}}^{(k)} = c_f$  if  $q_{fn}^{(k)} \geq 0$  with

$$q_{fn}^{(k)} := -\frac{K_{fn}^{(k)}}{\mu(c_f^{(k)})} \left[ \frac{p_m^{(k)} - p_f}{\epsilon/2} - (\rho(c_f^{(k)}) - \rho_f) \mathbf{g} \cdot \mathbf{n}^{(k)} \right], \quad x \in \mathcal{S}^{(k)}. \quad (6)$$

In (6),  $K_{fn}^{(k)} : \mathcal{S}^{(k)} \rightarrow \mathbb{R}$  is the normal permeability and  $D_{fn}^{(k)} : [0, +\infty) \times \mathcal{S}^{(k)} \rightarrow \mathbb{R}$  is the normal diffusion and dispersion coefficient of the fracture – bulk medium interface  $\mathcal{S}^{(k)}$ .

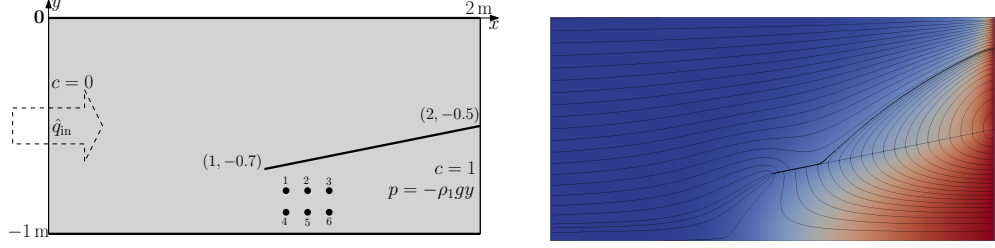


**Fig. 1:** Left: Geometry, boundary conditions and the selected points for the modified Henry problem with a fracture. Right: The flow pattern of this problem; color:  $c_m$  (red for  $c_m = 1$ ); black lines: streamlines of the flow field.

Systems (1) and (3) are coupled by the continuity of the mass fluxes of the interfaces  $\mathcal{S}^{(k)}$ ,  $k \in \{1, 2\}$ :

$$\left. \begin{aligned} \rho(c_m^{(k)}) \mathbf{q}_m \cdot \mathbf{n}^{(k)} &= Q_{fn}^{(k)} \\ \rho(c_m^{(k)}) \mathbf{D}_m \nabla c_m \cdot \mathbf{n}^{(k)} &= P_{fn}^{(k)} \end{aligned} \right\}, \quad x \in \mathcal{S}^{(k)} \quad (7)$$

Furthermore, for the inner edges of fractures, we impose the no-flux boundary conditions so that no mass exchange is possible there, cf. [20, 21].

Equations (1), (3) and (7) with the velocities (2), (4) and (6) as well as particular specifications of the parameters  $\rho$ ,  $\mu$ ,  $\phi_{m,f}$ ,  $\mathbf{K}_m$ ,  $\mathbf{D}_m$ ,  $K_f$ ,  $K_{fn}$ ,  $D_f$  and  $D_{fn}$  form the complete model for the density-driven flow in the porous medium. This system must be closed by boundary conditions for  $c_m$ ,  $c_f$ ,  $p_m$  and  $p_f$  on  $\partial\mathcal{D}$  as well as initial conditions for  $c_m$  and  $c_f$  at  $t = 0$ .

## 2.2 Model problem settings

For our numerical tests, we choose a simple but very illustrative two-dimensional problem with one fracture, proposed in [20]. It extends the setting of the Henry problem [25, 43] with a fracture. The aquifer is represented by a rectangular domain  $\mathcal{D} = [0, 2] \times [-1, 0]$  [m<sup>2</sup>] completely saturated with the liquid phase, see Fig. 1 (left). The fracture is located near the right “sea side” where the heavy salty water intrudes into the aquifer and cuts this boundary.

The model presented in Section 2.1 must be closed by specification of boundary conditions for  $c_{m,f}$  and  $p_{m,f}$ , as well as initial conditions for  $c_{m,f}$ . In this work, we follow the settings from [20] but add the uncertainty as described in Section 2.3 below. In particular, for the initial conditions, we set

$$c_m|_{t=0} = 0, \quad c_f|_{t=0} = 0. \quad (8)$$

A scheme of the boundary conditions is shown in Fig. 1 (left). On the right boundary, the Dirichlet conditions for  $c_{m,f}$  and  $p_{m,f}$  model the seawater intrusion:

$$c_{m,f}|_{x=2} = 1, \quad p_{m,f}|_{x=2} = -\rho_1 g y. \quad (9)$$

On the left boundary, the inflow (recharge) of fresh water is imposed:

$$c_m|_{x=0} = 0, \quad \rho \mathbf{q}_m \cdot \mathbf{e}_x|_{x=0} = \hat{q}_{\text{in}}, \quad (10)$$

where  $\mathbf{e}_x = (1, 0)^\top$ , and  $\hat{q}_{\text{in}}$  is a prescribed function of time, see Sect. 2.3. Note that the fracture does not cut the left side of the domain, so no boundary conditions for  $c_f$  and  $p_f$  are required there. For the upper and the lower boundaries of  $\mathcal{D}$ , we impose no-flux boundary conditions for all the equations.

The flow and salt transport patterns appearing in this problem are discussed in [20]. They are presented in Fig. 1 (right): The color codes the mass fraction  $c_m$  with red corresponding to  $c_m = 1$  and blue to  $c_m = 0$ ; the lines are the streamlines of the flow. In the left part of  $\mathcal{D}$ , the flow is induced by the pure water recharge through the left boundary. As in the Henry problem, the salt water intruding through the lower part of the right boundary turns up and is washed out through the upper part of the right side. In particular, the much more permeable fracture serves as a pathway for the strong wash-out that evacuates the salty water from the domain. For that, the part of the domain below the fracture is mostly separated from the upper part of the domain — as much as the capacity of the fracture allows. These phenomena depend on the width and the permeability of the fracture. In this work, we investigate how the fracture aperture influences the concentration.

In the case of time-independent boundary conditions, the mass fraction field converges to a steady state (cf. [20]). However, before it, there is an initial instationary phase taking considerable time when the maximum uncertainty in the solution w.r.t. the parameters is attained. This phase can be recognized even for the time-dependent recharge  $\hat{q}_{\text{in}}$  considered below.

In this paper, as for the Henry problem (see [42, 43, 50]), we set

$$\rho(c) = \rho_0 + (\rho_1 - \rho_0)c, \quad \mu = \text{const}, \quad (11)$$

where  $\rho_0$  is the density of the pure water and  $\rho_1$  is the density of the brine (both considered as constants). Besides that, we assume that porous medium is isotropic:

$$\mathbf{K}_m = K_m \mathbf{I}, \quad (12)$$

where  $K_m : \mathcal{M} \rightarrow \mathbb{R}$ . Furthermore, in this work, we neglect the mechanical dispersion, so that

$$\mathbf{D}_m = \phi_m D_{\text{mol}} \mathbf{I}, \quad \mathbf{D}_f = \phi_f D_{\text{mol}} \quad (13)$$

where  $D_{\text{mol}} \in \mathbb{R}$  is the constant molecular diffusion coefficient of the salt in the liquid phase. For the interface between the bulk medium and the fracture, we assume

$$K_{fn} = K_m, \quad D_{fn} = \phi_m D_{\text{mol}}, \quad x \in \mathcal{S}. \quad (14)$$

Deterministic values of these parameters that are not varied in the scenarios are presented in Table 1.

We investigate the mass fraction  $c_m$  at 6 locations where the largest variance is observed. This corresponds to the situation when the water quality of wells reaching these points is controlled. The list of selected points follows (see Fig. 1):

$$\{\mathbf{x}_i := (x_i, y_i)_{i=1,\dots,6}\} = \{(1.1, -0.8), (1.2, -0.8), (1.3, -0.8), \\ (1.1, -0.9), (1.2, -0.9), (1.3, -0.9)\} \quad (15)$$

Whereas the other points can be considered, the reason to select these 6 points (and 6 small subdomains) is that not all other points are “interesting”, i.e., not all points have significant variation in  $c_m$ . MLMC reduces the variance, but if the initial variance is small, there is no need to use MLMC.

Symbol	Quantity	Value	Unit
$D_{\text{mol}}$	Deterministic diffusion coefficient in the medium	$18.8571 \cdot 10^{-6}$	$[\text{m}^2 \text{s}^{-1}]$
$\mathbf{g}$	Gravity	9.8	$[\text{m s}^{-2}]$
$K_m$	Deterministic permeability of the medium	$1.019368 \cdot 10^{-9}$	$[\text{m}^2]$
$K_f$	Deterministic permeability of the fracture	$1.019368 \cdot 10^{-6}$	$[\text{m}^2]$
$\phi_m$	Deterministic porosity of the medium	0.35	-
$\phi_f$	Deterministic porosity of the fracture	0.7	-
$\mu$	Viscosity	$10^{-3}$	$[\text{kg m}^{-1} \text{s}^{-1}]$
$\rho^{pW}$	Density of water	$1 \cdot 10^3$	$[\text{kg m}^{-3}]$
$\rho^{pB}$	Density of brine	$1.025 \cdot 10^3$	$[\text{kg m}^{-3}]$
$\epsilon$	Fracture width	$\mathbb{E}[\epsilon] = 5.05 \cdot 10^{-3}$	$[\text{m}]$

**Table 1:** Simulation parameters for the model problem from Section 2.2

### 2.3 Stochastic modeling of porosity, permeability and fracture width

Stochastic modeling is used to simulate the behavior of a fractured reservoir under uncertainty. The primary sources of uncertainty are the hydrogeological properties of the porous medium — porosity ( $\phi_{m,f}$ ) and permeability ( $K_{m,f}$ ) fields of the porous matrix and the fracture aperture ( $\epsilon$ ) — as well as the freshwater recharge intensity  $\hat{q}_x$ . In this work we do not consider the uncertainty in  $\phi_f$  and  $K_f$ . The QoIs are related to the mass fraction  $c_m$ , a function of  $\phi_m$ ,  $K_m$ , and  $\hat{q}_x$ . We model the uncertain  $\phi_m$  using a random field and assume  $K_m$  to dependent on  $\phi_m$ :

$$K_m = K_m(\phi_m) \in \mathbb{R}. \quad (16)$$

The distribution of  $\phi(\mathbf{x}, \boldsymbol{\xi})$ ,  $\mathbf{x} \in \mathcal{D}$ , is determined by a set of stochastic parameters  $\boldsymbol{\xi} = (\xi_1, \dots, \xi_M, \dots)$ . Each component  $\xi_i$  is a random variable.

The dependence in (16) is specific for every material. We refer to [11, 34, 35] for a detailed discussion. In this work, we use a Kozeny-Carman-like law

$$K_m(\phi_m) = \kappa_{KC} \cdot \frac{\phi_m^3}{1 - \phi_m^2}, \quad (17)$$



where  $\kappa_{KC}$  is a constant scaling factor. The recharge inflow flux is kept constant across the left boundary but depends on the stochastic variable  $\hat{q}_x$ . We also assume that it is independent of  $\phi$  and  $\mathbf{K}$ .

The uncertain width of the fracture, the recharge, and the porosity are modeled as follows,  $\xi_1, \xi_2, \xi_3 \in U[-1, 1]$ ,

$$\epsilon(\xi_1) = 0.01 \cdot ((1 - 0.01) \cdot \xi_1 + (1 + 0.01))/2, \quad (18)$$

$$\hat{q}_x(t, \xi_3) = 3.3 \cdot 10^{-6} \cdot (1 + 0.1\xi_3)(1 + 0.1 \sin(\pi t/40)), \quad (19)$$

$$\phi_m(x, y, \xi_2) = 0.35 \cdot (1 + 0.02 \cdot (\xi_2 \cos(\pi x/2) + \xi_2 \sin(2\pi y))). \quad (20)$$

The corresponding permeability is defined by (17).

Unknown porosity can be also modeled by a random field. One of the ways to compute this random field is to make an assumption about the covariance matrix or to estimate it from the available measurement data. Then an auxiliary eigenvalue problem is solved and the truncated Karhunen-Loève expansion (KLE) is constructed [29]. Due to the high complexity of this approach, we implement a simpler one. We use  $L_2$  orthogonal functions ( $\sin()$  and  $\cos()$ ), which mimic the  $L_2$ -orthogonal functions used in the KLE. These functions are then multiplied by the uniform random variables  $\xi$  as in (20). Typically one takes one of three options for  $\xi$ : uniform, Gaussian or log-normal.

## 3 Numerical Methods

### 3.1 Numerical methods for the deterministic problem

The system (1)-(3) is numerically solved in the domain  $\mathcal{D} \times [0, T]$ .  $\mathcal{D}$  is covered with an unstructured grid  $\mathcal{D}_h$  of triangles and quadrilaterals. We denote the characteristic mesh size by  $h$ . We apply a special technique for resolving the jump of the solution at the fracture, cf. [36] for details. The vertex-centered finite-volume scheme is used for the discretization of the system (1-4) in space (cf. [36, 38]). The number of degrees of freedom associated with  $\mathcal{D}_h$  is denoted by  $n$ . There are two degrees of freedom per grid vertex in  $\mathcal{D}_h$ : one for the mass fraction  $c_{m,f}$  and another for the pressure  $p$ . At the fracture, several grid vertices share the same geometrical position, cf. [36, 38]. We use the regular refinement to create the grid hierarchy so that  $h = \mathcal{O}(n^{-1/d})$ . The implicit Euler method with a time step  $\tau$  is used for the time discretization of (1-4). The number of the computed time steps is  $r = T/\tau$ . In this paper, we focus on the mass fraction  $c_m$  of the salt in the bulk porous medium. We denote the part of the discrete solution of the model approximating  $c_m$  by  $c_{m,h,\tau}$ .

We use the full upwind for the convective terms (cf. [15]). Therefore, the discretization error is of the first order w.r.t. the spatial mesh size  $h$ . Furthermore, the Euler method provides the first-order discretization error w.r.t.  $\tau$ . Thus, as  $d = 2$ ,

$$\|c_m - c_{m,h,\tau}\|_2 = \mathcal{O}(h + \tau) = \mathcal{O}(n^{-1/2} + r^{-1}), \quad (21)$$

which is consistent with our numerical tests.

The implicit time-stepping scheme is unconditionally stable but requires solution of the extensive nonlinear discretized algebraic system with  $n$  unknowns in every time step. The Newton's method is used for this. Linear systems in the Newton iteration are solved using the BiCGStab method (cf. [2]) preconditioned with the geometric multigrid method (V-cycle, cf. [22]). In the multigrid cycle, the  $ILU_\beta$ -smothers [23] and Gaussian elimination are used as the coarse grid solver.

### 3.2 MLMC Algorithm

To reduce the total computing cost, we apply the MLMC method, which is a natural idea because the deterministic solver uses a multigrid method (see Section 3.1). The MLMC method gains efficiency by combining samples computed on different grids in the hierarchy. A more in-depth description of these techniques is found in [9, 10, 17, 18, 24, 30, 47].

Let  $\xi$  be a vector of random variables, and  $g(\xi)$  the quantity of interest. In this work, we tried different QoI  $g$ : solution  $c_m$  at a point  $(t, \mathbf{x})$ , integrals over a small subdomain  $\Delta_i$  and over the whole computational domain  $\mathcal{D}$ , see Sect. 4. The MLMC method aims to approximate the expected value  $\mathbb{E}[g]$  with an optimal computational cost. MLMC constructs a telescoping sum, defined over a sequence of spatial and temporal meshes,  $\ell = 0, \dots, L$ , as described next, to achieve this goal. The QoI  $g$ , numerically evaluated on level  $\ell$ , is denoted by  $g_{h_\ell, \tau_\ell, \ell}$  or, for simplicity, by just  $g_\ell$ , where  $h_\ell$  and  $\tau_\ell$  are the discretization steps in space and time on level  $\ell$ .

Let  $s_0$  denote the maximum computational cost of the evaluation of one realization of  $g_0$ . Similarly,  $s_\ell$  denotes the computing cost of evaluating  $g_\ell - g_{\ell-1}$ . For simplicity, we assume that  $s_\ell$  for  $g_\ell - g_{\ell-1}$  is almost the same as  $s_\ell$  for  $g_\ell$ . Since the number of required iterations is variable, the cost of computing a sample of  $g_\ell - g_{\ell-1}$  may fluctuate for various realizations.

The MLMC method calculates  $\mathbb{E}[g_L] \approx \mathbb{E}[g]$  using the following telescopic sum:

$$\mathbb{E}[g_L] = \mathbb{E}[g_0] + \sum_{\ell=1}^L \mathbb{E}[g_\ell - g_{\ell-1}] \quad (22)$$

$$\approx m_0^{-1} \sum_{i=1}^{m_0} g_0^{(0,i)} + \sum_{\ell=1}^L \left( m_\ell^{-1} \sum_{i=1}^{m_\ell} (g_\ell^{(\ell,i)} - g_{\ell-1}^{(\ell,i)}) \right). \quad (23)$$

In the above equation, level  $\ell$  in the superscript  $(\ell, i)$  indicates that independent samples are used at each correction level.

As  $\ell$  increases, the variance of  $g_\ell - g_{\ell-1}$  decreases. Thus, the total computational cost can be reduced by taking fewer samples on finer meshes.

In the following numerical experiments  $n_\ell = 4n_{\ell-1} = \dots = 4^\ell n_0 = 2^{d\ell} n_0$ ,  $d = 2$ , and  $r_\ell = 2r_{\ell-1} = \dots = 2^\ell r_0$ . In the case of uniform, equidistant mesh, we could also write similar formulas for step sizes:  $h_\ell = h_{\ell-1} \cdot 2^{-1} = h_{\ell-2} \cdot 2^{-2} = \dots = h_0 \cdot 2^{-\ell}$  and  $\tau_\ell = \tau_0 \cdot 2^{-\ell}$ .

The average cost  $s_\ell$  of generating one sample of  $g_\ell$  (the cost of one deterministic simulation for one random realization) is

$$s_\ell = \mathcal{O}(n_\ell r_\ell) = \mathcal{O}(4^\ell n_0 \cdot 2^\ell r_0) = \mathcal{O}(2^{2\ell} n_0 \cdot 2^\ell r_0) = \mathcal{O}(2^{\hat{d}\ell\gamma} n_0 r_0), \quad (24)$$

where  $\hat{d} = d + 1 = 3$  and  $\gamma = 1$ .

**Definition 1.** Let  $Y_\ell := m_\ell^{-1} \sum_{i=1}^{m_\ell} (g_\ell^{(\ell,i)} - g_{\ell-1}^{(\ell,i)})$ , where  $g_{-1} \equiv 0$ , so that

$$\mathbb{E}[Y_\ell] := \begin{cases} \mathbb{E}[g_0], & \ell = 0 \\ \mathbb{E}[g_\ell - g_{\ell-1}], & \ell > 0 \end{cases}. \quad (25)$$

Denote by  $Y := \sum_{\ell=0}^L Y_\ell$  the multilevel estimator of  $\mathbb{E}[g]$  based on  $L+1$  levels and  $m_\ell$  independent samples on level  $\ell$ , where  $\ell = 0, \dots, L$ .

Furthermore, we denote  $V_0 = \mathbb{V}[g_0]$  and for  $\ell \geq 1$ , let  $V_\ell$  be the variance of  $g_\ell - g_{\ell-1}$ :  $V_\ell := \mathbb{V}[g_\ell - g_{\ell-1}]$ .

The standard theory states the following facts for the mean and the variance:

$$\mathbb{E}[Y] = \mathbb{E}[g_L], \quad \mathbb{V}[Y] = \sum_{\ell=0}^L m_\ell^{-1} V_\ell. \quad (26)$$

The cost of the multilevel estimator  $Y$  is

$$S := \sum_{\ell=0}^L m_\ell s_\ell. \quad (27)$$

The mean squared error (MSE) is used to measure the quality of the multilevel estimator:

$$\text{MSE} := \mathbb{E}[(Y - \mathbb{E}[g])^2] = \mathbb{V}[Y] + (\mathbb{E}[Y] - \mathbb{E}[g])^2, \quad (28)$$

where  $Y$  is what we computed via MLMC, and  $\mathbb{E}[g]$  what actually should be computed. To achieve

$$\text{MSE} \leq \varepsilon^2$$

for some prescribed tolerance  $\varepsilon$ , we ensure that

$$(\mathbb{E}[Y] - \mathbb{E}[g])^2 = (\mathbb{E}[g_L - g])^2 \leq \frac{1}{2}\varepsilon^2 \quad (29)$$

and

$$\mathbb{V}[Y] \leq \frac{1}{2}\varepsilon^2. \quad (30)$$

The bias error  $\mathbb{E}[g_L - g]$  corresponds to the discretization error discussed in Sec. 3.1. Later we will see that  $\mathbb{E}[Y] - \mathbb{E}[g] = \mathcal{O}(2^{-\alpha L})$  with  $\alpha \approx 1$ . The bias error can be made smaller than  $\varepsilon^2/2$  by choosing a sufficiently large  $L$ . Then, for this  $L$ , we can compute optimal  $m_0, \dots, m_L$  by formula in (34) to provide (30).

In the following, we repeat the well-known [18] results on the computation of the sequence  $m_0, \dots, m_L$ . For a fixed variance  $\mathbb{V}[Y] =: \varepsilon^2/2$ , the cost  $S$  is minimized by choosing as  $m_\ell$  the solution of the optimization problem

$$\min_{m_0, \dots, m_L} F(m_0, \dots, m_L), \quad (31)$$

where  $F(m_0, \dots, m_L) := \sum_{\ell=0}^L \left( m_\ell s_\ell + \mu^2 \frac{V_\ell}{m_\ell} \right)$ ,  $\mu^2$  is a Lagrange multiplier. Thus, the derivatives of  $F$  w.r.t.  $m_\ell$  are equal to zero:

$$\frac{\partial F(m_0, \dots, m_L)}{\partial m_\ell} := s_\ell - \mu^2 \frac{V_\ell}{m_\ell^2} = 0. \quad (32)$$

Solving the system (32), we obtain

$$m_\ell^2 = \mu^2 \frac{V_\ell}{s_\ell}, \quad \text{i.e.} \quad m_\ell = \mu \sqrt{\frac{V_\ell}{s_\ell}}. \quad (33)$$

Taking into account that the variation  $\mathbb{V}[Y]$  is fixed and substituting (33) into (26), i.e.  $\sum_{\ell=0}^L V_\ell/m_\ell = \varepsilon^2/2$ , we obtain an equation for  $\mu$ :

$$\sum_{\ell=0}^L \frac{V_\ell}{\mu \sqrt{\frac{V_\ell}{s_\ell}}} = \frac{1}{2} \varepsilon^2.$$

From this equation, we get  $\mu = 2\varepsilon^{-2} \sum_{\ell=0}^L \sqrt{V_\ell s_\ell}$ , and therefore

$$m_\ell = 2\varepsilon^{-2} \cdot \sqrt{\frac{V_\ell}{s_\ell}} \cdot \sum_{i=0}^L \sqrt{V_i s_i}. \quad (34)$$

For this set of  $m_\ell$ , the total computational cost of  $Y$  is

$$S = 2\varepsilon^{-2} \left( \sum_{\ell=0}^L \sqrt{V_\ell s_\ell} \right)^2. \quad (35)$$

For further analysis of this sum, see [18], p.4.

The cost increases exponentially with  $\ell$  while the weak error  $\mathbb{E}[g_L - g]$  and multi-level correction variance  $V_\ell$  decrease exponentially leads to the following theorem (cf. Theorem 1, p. 6 in [18]):

**Theorem 2.** *Consider a fixed  $t = t^*$ . Suppose positive constants  $\alpha, \beta, \gamma > 0$  exist such that  $\alpha \geq \frac{1}{2} \min(\beta, \gamma \hat{d})$ , and*

$$|\mathbb{E}[g_\ell - g]| \leq c_1 2^{-\alpha \ell} \quad (36a)$$

$$V_\ell \leq C_2 2^{-\beta \ell} \quad (36b)$$

$$s_\ell \leq c_3 2^{\hat{d} \gamma \ell}. \quad (36c)$$

Then, for any accuracy  $\varepsilon < e^{-1}$ , a constant  $c_4 > 0$  and a sequence of realizations  $\{m_\ell\}_{\ell=0}^L$  exist, such that  $MSE < \varepsilon^2$ , where  $MSE$  is defined in (28), and the

computational cost is

$$S = \begin{cases} c_4 \varepsilon^{-2}, & \beta > \hat{d}\gamma \\ c_4 \varepsilon^{-2} (\log(\varepsilon))^2, & \beta = \hat{d}\gamma \\ c_4 \varepsilon^{-(2 + \frac{\hat{d}\gamma - \beta}{\alpha})}, & \beta < \hat{d}\gamma. \end{cases} \quad (37)$$

This theorem (see also [8, 9, 17, 26, 27]) indicates that, even in the worst-case scenario, the MLMC algorithm has a lower computational cost than that of the traditional (single-level) MC method, which scales as  $\mathcal{O}(\varepsilon^{-2 - \hat{d}\gamma/\alpha})$ .

**Remark 1.** In Theorem 2, the factors  $C_1, C_2, C_3, C_4$  as well as the exponents  $\alpha, \beta$  and  $\gamma$  depend on the time point  $t$ . This makes  $L$  and  $m_\ell$  time-dependent, too.

**Remark 2.** One possible choice for a scaling factor in (29) and (30) is  $E_0 := |\mathbb{E}[g_0(t^*, \mathbf{x}^*)]|$ , where  $g_0(t^*, \mathbf{x}^*)$  is the solution computed on level  $\ell = 0$  at point  $(t^*, \mathbf{x}^*)$ .

**Remark 3.** We consider the error relatively to  $g$ . For this, in (29) and (30), we replace  $\varepsilon$  by  $\varepsilon \cdot E_0$ . Equivalently, we can divide (rescale)  $\mathbb{E}[g_L - g]$  by  $E_0$  and  $V_i$  by  $E_0^2$ . Therefore, we get:

$$|\mathbb{E}[g_L - g]| \leq C_1 2^{-\alpha L}. \quad (38)$$

Now, to satisfy (29), we want

$$|\mathbb{E}[g_L - g]| \leq \frac{1}{\sqrt{2}} \varepsilon E_0. \quad (39)$$

From this inequality, we can estimate  $L$ :

$$C_1 2^{-\alpha L} = \frac{\varepsilon E_0}{\sqrt{2}} \quad (40)$$

$$L = -\frac{1}{\alpha} \log_2 \frac{\varepsilon E_0}{\sqrt{2} C_1}. \quad (41)$$

Equations (34) and (35) attain the form

$$m_\ell = \frac{2\varepsilon^{-2}}{E_0^2} \cdot \sqrt{\frac{V_\ell}{s_\ell}} \cdot \sum_{i=0}^L \sqrt{V_i s_i}, \quad S = \frac{2\varepsilon^{-2}}{E_0^2} \left( \sum_{\ell=0}^L \sqrt{V_\ell s_\ell} \right)^2. \quad (42)$$

Using preliminary numerical tests (see Fig. 5) and following preprocessing steps as in Algorithm 1, we can estimate the convergence rates  $\alpha$  for the mean (the so-called weak convergence) and  $\beta$  for the variance (the so-called strong convergence), as well as the constants  $C_1$  and  $C_2$ . In addition,  $\alpha$  is strongly connected to the order of the discretization error (see Section 3.1), which equals 1. Note that precise estimates of parameters  $\alpha$  and  $\beta$  are crucial to distribute the computational effort optimally.

---

**Algorithm 1** Preprocessing for MLMC algorithm

---

Input:  $L = 3$ ,  $m_\ell = 10$ ,  $\ell = 0, \dots, L$   
Compute  $g_\ell(\omega_i)$ ,  $g_\ell(\omega_i) - g_{\ell-1}(\omega_i)$  for  $i = 1 \dots m_\ell$  and  $\ell = 1 \dots L$   
Estimate  $\mathbb{E}[g_\ell(\omega_i) - g_{\ell-1}(\omega_i)]$ ,  $\mathbb{V}[g_\ell(\omega_i) - g_{\ell-1}(\omega_i)]$   
Estimate convergence rates  $\alpha$  and  $\beta$ , complexity rate  $\gamma$ , constants  $C_1, C_2, C_3$

---

---

**Algorithm 2** MLMC algorithm

---

Input: MSE Error  $\varepsilon^2$   
Estimate  $L$   
Compute  $m_\ell$ ,  $\ell = 0, \dots, L$   
Compute  $\mathbb{E}[g_\ell(\omega_i) - g_{\ell-1}(\omega_i)]$ ,  $i = 1 \dots m_\ell$   
Build the telescopic sum to estimate  $\mathbb{E}[g]$

---

## 4 Numerical Experiments

We performed numerical experiments with four uncertain parameters: thickness, recharge, permeability and porosity. Permeability and porosity are mutually dependent. To check that uncertainties in all four parameters contribute significantly to the solution, we performed auxiliary experiments with only 1-2 random parameters. First, only one of these four parameters was uncertain, then thickness and recharge were uncertain. In this way we checked that there were no parameters whose contribution could be neglected.

We consider the following QoIs: 1) the solution  $c_m$  at a point  $(t, \mathbf{x})$ , i.e.  $g = c_m(t, \mathbf{x})$ , and 2) an integral over a small sub-domain

$$I_i(t, \omega) := \int_{\mathbf{x} \in \Delta_i} c_m(t, \mathbf{x}, \omega) \rho(c_m(t, \mathbf{x}, \omega)) d\mathbf{x}, \quad \text{where} \quad (43)$$

$$\Delta_i := [x_i - 0.1, x_i + 0.1] \times [y_i - 0.1, y_i + 0.1], \quad i = 1, \dots, 6. \quad (44)$$

The list of all points  $\mathbf{x}_i = (x_i, y_i)$  is defined in (15). The value of  $I_i$  is the mass of the salt in a subdomain  $\Delta_i$ . The size of each  $\Delta_i$  is small ( $0.2^2 = 0.04$ ), compared to  $\mathcal{D}$ .

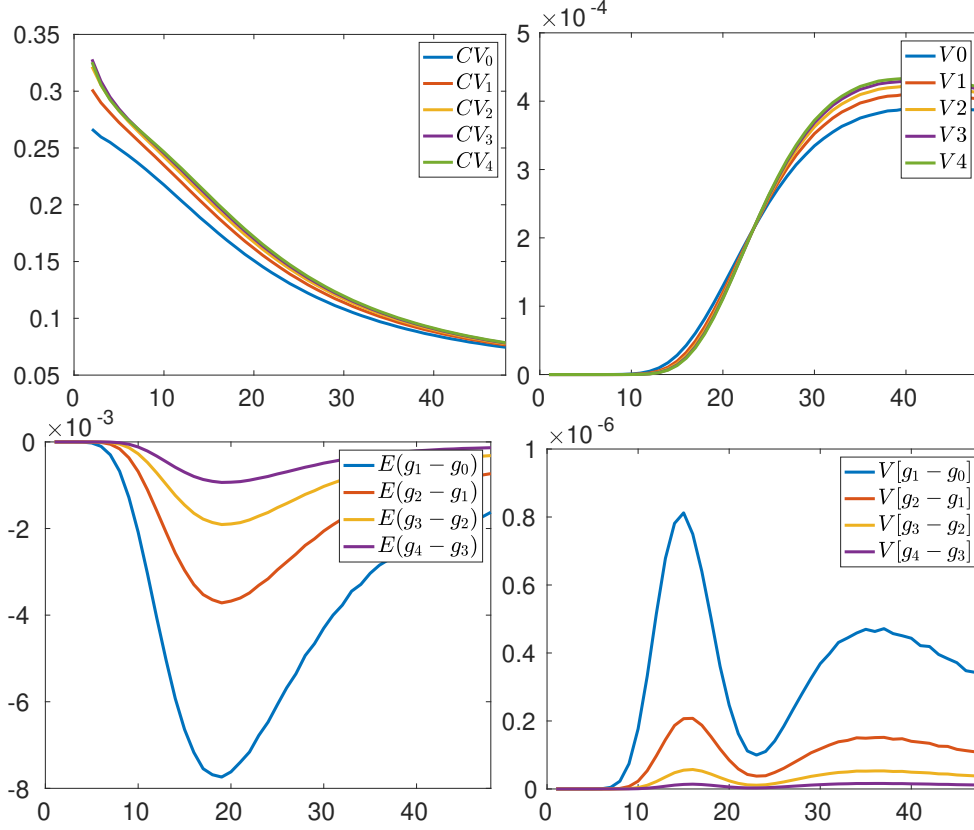
The numerical scheme provides only the first order of the accuracy to compute  $c_m(t, \mathbf{x}_i, \omega)$  and  $I_i(t, \omega)$ , i.e., the convergence rate  $\alpha$  (weak convergence in (36a)) should be  $\approx 1$ . The numerical results below show that, indeed,  $\alpha \approx 1$ .

Table 2 contains computing times needed to compute the solution  $c_m$  at each level  $\ell$ . The fifth column contains the average computing time, and the sixth and seventh columns contain the shortest and longest computing times. The computing time for each simulation varies depending on the number of iterations, which depends on the porosity and permeability. We observed that, after  $\approx 6016$  sec., the solution is almost unchanging; thus, we perform the experiment only for  $t \in [0, T]$ , where  $T = 6016$  sec. For example, if the number of time steps is  $r_\ell = 188$  (Level 0 in Table 2), then the time step  $\tau = \frac{T}{r_\ell} = \frac{6016}{188} = 32$  sec.

In Figure 2 (top left) we visualise the coefficient of variation  $CV(g)$ , which is the ratio of the standard deviation to the mean. The variance  $V_\ell := \mathbb{V}[g_\ell]$  is shown on the

Level $\ell$	$n_\ell, (\frac{n_\ell}{n_{\ell-1}})$	$r_\ell, (\frac{r_\ell}{r_{\ell-1}})$	$\tau_\ell = 6016/r_\ell$	Computing times ( $s_\ell$ ), $(\frac{s_\ell}{s_{\ell-1}})$		
				average	min.	max.
0	608	188	32	3	2.4	3.4
1	2368 (3.9)	376 (2)	16	22 (7.3)	15.5	27.8
2	9344 (3.9)	752 (2)	8	189 (8.6)	115	237
3	37120 (4)	1504 (2)	4	1831 (10)	882	2363
4	147968 (4)	3008 (2)	2	18580 (10)	7865	25418

**Table 2:** Number of degrees of freedom  $n_\ell$ , number of time steps  $r_\ell$ , step size in time  $\tau_\ell$ , average, minimal, and maximal computing times on each level  $\ell$ .



**Fig. 2:** (top left) The coefficient of variance  $CV_\ell := CV(g_\ell)$ , (top right) the variance  $\mathbb{V}[g_\ell]$ , (bottom left) the mean  $\mathbb{E}[g_\ell - g_{\ell-1}]$ , (bottom right) the variance  $\mathbb{V}[g_\ell - g_{\ell-1}]$ . The QoI is  $g = c_m(t, \mathbf{x}_1)$ . The small oscillations in the two lower pictures are due to the dependence of the recharge  $\hat{q}_x$  on the time, cf. (19).

top right, the mean  $\mathbb{E}[g_\ell - g_{\ell-1}]$  on the bottom left and the variance  $\mathbb{V}[g_\ell - g_{\ell-1}]$  on the bottom right. The QoI is  $g := c_m(t, \mathbf{x}_1)$  and the time  $t = 0, \dots, 47\tau$  is along the  $x$  axis.

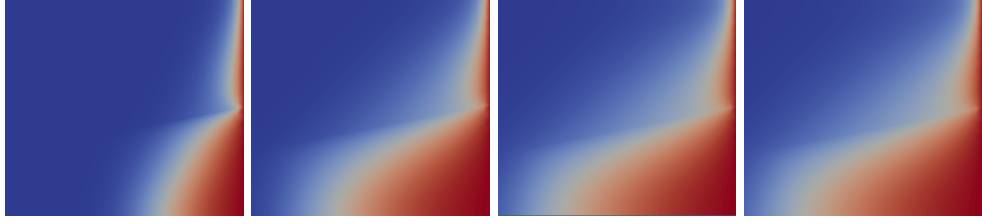


**Fig. 3:** The mean value  $\mathbb{E}[c_m(t, \mathbf{x})]$  at  $t = \{7\tau, 19\tau, 40\tau, 94\tau\}$ . In all cases,  $\mathbb{E}[c_m](t, \mathbf{x}) \in [0, 1]$ .

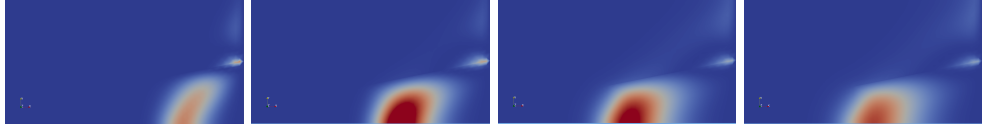


**Fig. 4:** The variance  $\mathbb{V}[c_m(t, \mathbf{x})]$  at  $t = \{7\tau, 19\tau, 40\tau, 94\tau\}$ . Maximal values (dark red colour) of  $\mathbb{V}[c_m]$  are  $1.9 \cdot 10^{-3}$ ,  $3.4 \cdot 10^{-3}$ ,  $2.9 \cdot 10^{-3}$ ,  $2.4 \cdot 10^{-3}$  respectively. The dark blue colour corresponds to a zero value.

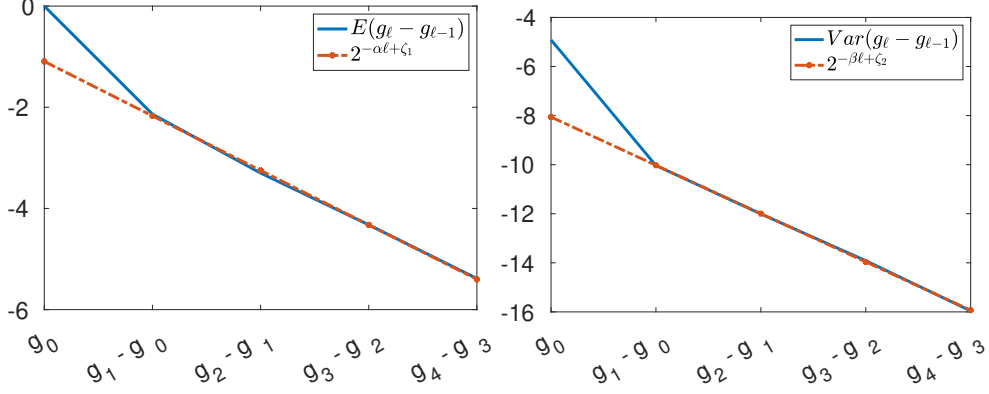
#### 4.1 The mean value and variance

Fig. 3 shows the mean value  $\mathbb{E}[c_m(t, \mathbf{x})]$  at time points  $\{7\tau, 19\tau, 40\tau, 94\tau\}$ . In all cases  $\mathbb{E}[c_m(t, \mathbf{x})] \in [0, 1]$ , the dark red color corresponds to the value 1 and dark blue to the value 0.

Similarly, Fig. 4 presents the variance of the salt mass fraction in the computational domain for  $t = \{7\tau, 19\tau, 40\tau, 94\tau\}$ . The maximal values of  $\mathbb{V}[c_m]$  (denoted by the dark red colour) are  $1.9 \cdot 10^{-3}$ ,  $3.4 \cdot 10^{-3}$ ,  $2.9 \cdot 10^{-3}$ ,  $2.4 \cdot 10^{-3}$  respectively.

The general flow and transport patterns in this setting were discussed in Sect. 2.2. The aperture  $\epsilon$  of the fracture has the most essential influence on the  $c_m$ . If  $\epsilon$  is small (i.e. for  $\xi_1 = -1$ , cf. (18)), the fracture does not increase the permeability of the medium significantly so the flow and transport are very similar to the Henry problem. For thick fractures ( $\xi_1 = 1$ ), the separation of the upper and the lower part of the domain (see Sect. 2.2) is very strong. This is clearly visible in the mean value of  $c_m(t, \mathbf{x})$  in Fig. 3. Note that  $\epsilon$  changes the flow under the left end of the fracture where fluid enters it. This area is characterized by the high value of the variance, see Fig. 4. The influence of the other uncertainties is weaker but nevertheless important, too.





**Fig. 5:** The weak and the strong convergences, QoI is  $g := c_m(t_{15}, \mathbf{x}_1)$ ,  $\alpha = 1.07$ ,  $\zeta_1 = -1.1$ ,  $\beta = 1.97$ ,  $\zeta_2 = -8$ .

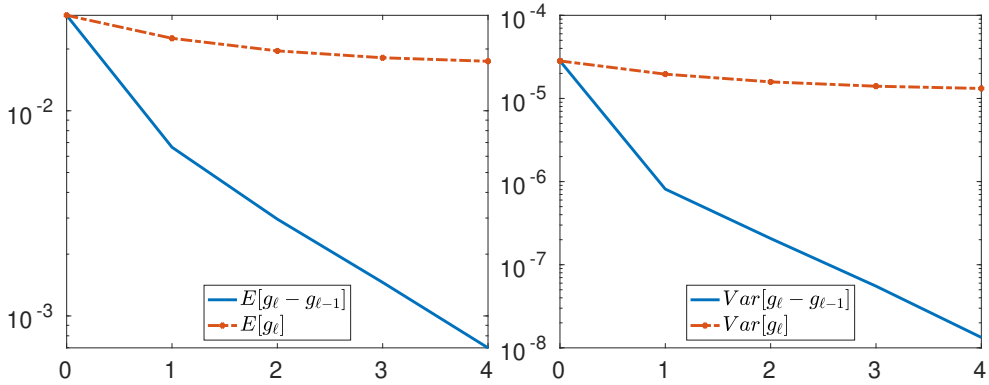


**Fig. 6:** Decay comparison of (left)  $\mathbb{E}[g_\ell - g_{\ell-1}]$  and  $\mathbb{E}[g_\ell]$  vs.  $\ell$ ; (right)  $\mathbb{V}[g_\ell - g_{\ell-1}]$  and  $\mathbb{V}[g_\ell]$ . QoI  $g = c_m(t_{18}, \mathbf{x}_1)$ ,  $\mathbf{x}_1 = (1.1, -0.8)$ .

## 4.2 Estimation of convergence rates $\alpha$ and $\beta$ for various QoIs

Figure 5 (left) shows the decay of  $\mathbb{E}[g_\ell - g_{\ell-1}]$  as a function of  $g_\ell - g_{\ell-1}$ . This dependence is fitted by a  $2^{-\alpha\ell + \zeta_1}$  function. The parameter  $\alpha$  indicates the weak convergence rate. Figure 5 (right) shows the decay of  $\mathbb{V}[g_\ell - g_{\ell-1}]$  with respect to  $g_\ell - g_{\ell-1}$ . This dependence is fitted by a  $2^{-\beta\ell + \zeta_2}$  curve, where the parameter  $\beta$  indicates the strong convergence rate. The constants are  $C_1 = 0.47$ ,  $C_2 = 3.7 \cdot 10^{-3}$ . The QoI is  $g := c_m(t_{15}, \mathbf{x}_1)$ . The calculated rates  $\alpha = 1.07$  and  $\beta = 1.97$  are very close to the theoretical values, which are 1 and 2 respectively.

In Fig. 6(left) the decays of  $\mathbb{E}[g_\ell - g_{\ell-1}]$  and  $\mathbb{E}[g_\ell]$  are plotted against the level  $\ell$ . The QoI is  $c_m(t_{18}, \mathbf{x}_1)$ ,  $\mathbf{x}_1 = (1.1, -0.8)$ . Similarly, Figure 6 (right) shows that  $\mathbb{V}[g_\ell - g_{\ell-1}]$  decays much faster than  $\mathbb{V}[g_\ell]$ . In Table 3 we provide estimations for the weak and strong convergence rates  $\alpha$  and  $\beta$ , as well as constants  $C_1$  and  $C_2$  for different QoIs. Each QoI is the solution at a point  $\mathbf{x}_i$  or an integral  $I_i$  as in (43). We

see that the value  $\alpha$  is very close to one. This is fully corresponding to the theory. The estimated value of  $\beta$  is also very close to the theoretical value, which is equal to  $2\alpha = 2$ . The values of  $\alpha$  and  $C_1$  are used for estimation of the number of needed levels  $L$ , see [31].

QoI	$\alpha$	$c_1$	$\beta$	$C_2$
$c_m(\mathbf{x}_1, 15\tau)$	-1.07	0.47	-1.97	$4 \cdot 10^{-3}$
$c_m(\mathbf{x}_2, 15\tau)$	-0.96	0.25	-1.6	$3.1 \cdot 10^{-4}$
$c_m(\mathbf{x}_3, 15\tau)$	-0.9	0.12	-1.9	$4.5 \cdot 10^{-5}$
$c_m(\mathbf{x}_4, 15\tau)$	-1.07	0.47	-1.94	$3.6 \cdot 10^{-3}$
$c_m(\mathbf{x}_5, 15\tau)$	-0.95	0.25	-1.5	$1.9 \cdot 10^{-4}$
$c_m(\mathbf{x}_6, 15\tau)$	-0.89	0.1	-1.82	$9.2 \cdot 10^{-5}$
$I_2(c_m)$	-1.5	8.3	-2.6	0.4

**Table 3:** Estimated the weak and strong convergence rates  $\alpha$  and  $\beta$ , and constants  $C_1$  and  $C_2$  for different QoIs. QoI are solution in a point  $\mathbf{x}_i$  and an integral  $I_i$  as in (43).

In Table 4 we show the numbers  $m_\ell$  needed to get the MSE error below  $\varepsilon^2$ , and  $\varepsilon$  should be understood as a relative error, as it is defined in (39). All numbers are obtained for the QoI  $g = c_m(t_{15}, \mathbf{x}_1)$ . The numbers  $m_{ell}$  can be very different for other QoIs.

$\varepsilon$	$m_0$	$m_1$	$m_2$	$m_3$	$m_4$
0.2	28	0	0	0	0
0.1	10	1	0	0	0
0.05	57	4	1	0	0
0.025	342	22	4	1	0
0.01	3278	205	35	6	1

**Table 4:** The number of samples  $m_\ell$  vs.  $\varepsilon$ , QoI  $g = c_m(t_{15}, \mathbf{x}_1)$ .

### 4.3 Comparison of MC and MLMC methods

In Figure 7 we compare the estimated costs of the MC (denoted by a blue dashed line) and MLMC (solid red line) methods, see the two bottom graphics. We also plot the  $\varepsilon^2$  graphic (yellow dashed line) and the theoretical MC and MLMC costs, purple dashed line and green dashed line respectively. The theoretical MC cost is  $\mathcal{O}(\varepsilon^{-2-\frac{\hat{d}\gamma}{\alpha}})$ , with  $\hat{d} = 2 + 1 = 3$ ,  $\gamma = 1$ ,  $\alpha = 1.08$ . One can see that from a certain epsilon  $\varepsilon \approx 8 \cdot 10^{-3}$  the MLMC outperforms the MC method. It can also be seen that the theoretical MC and MLMC lines (two top graphics) have the same slope as the calculated MC and MLMC lines (two bottom graphics). The theoretical MC and MLMC graphics are scaled by a constant for better visibility.

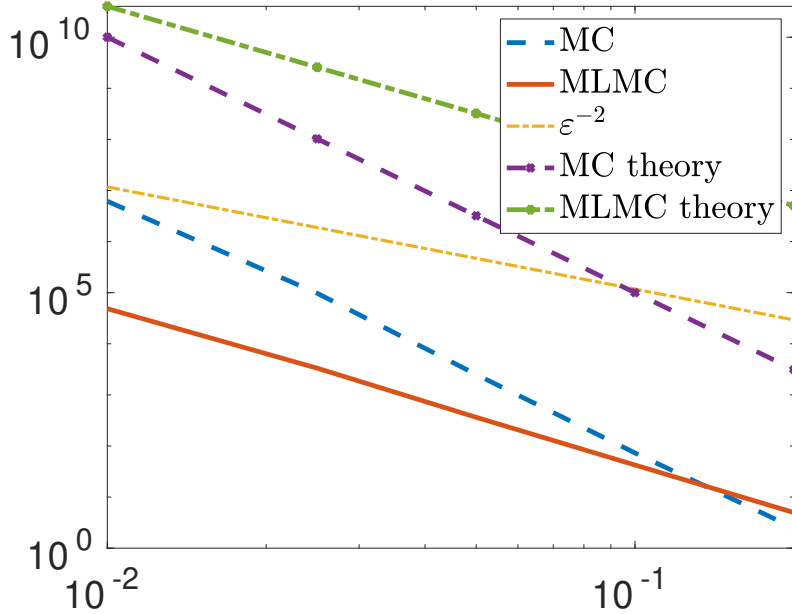


**Fig. 7:** Complexity comparison of ML and MLMC methods against  $\varepsilon$  (horizontal axis) in log-log scale.

## 5 Discussion and Conclusion

In this work we have considered a setting that mimics the Henry problem [42, 43], modeling seawater intrusion into a 2D coastal aquifer. The pure water recharge from the “land side” resists the salinisation of the aquifer due to the influx of saline water through the “sea side”, thereby achieving some equilibrium in the salt concentration. In our setting, following [20], we consider a fracture on the sea side that significantly increases the permeability of the porous medium.

The flow and transport essentially depend on the geological parameters of the porous medium, including the fracture. We investigated the effects of various uncertainties on saltwater intrusion. We assumed uncertainties in the fracture width, the porosity of the bulk medium, its permeability and the pure water recharge from the land side. The porosity and permeability were modeled by random fields, the recharge by a random but periodic intensity and the thickness by a random variable. We calculated the mean and variance of the salt mass fraction, which is also uncertain.

The main question we investigated in this work was how well the MLMC method can be used to compute statistics of different QoIs. We found that the answer depends on the choice of the QoI. First, not every QoI requires a hierarchy of meshes and MLMC. Second, MLMC requires stable convergence rates for  $\mathbb{E}[g_\ell - g_{\ell-1}]$  and  $\mathbb{V}[g_\ell - g_{\ell-1}]$ . These rates should be independent of  $\ell$ . If these convergence rates vary for different  $\ell$ , then it will be hard to estimate  $L$  and  $m_\ell$ , and MLMC will either not work or be suboptimal. We were not able to get stable convergence rates for all levels  $\ell = 1, \dots, 5$  when the QoI was an integral as in (43). We found that for  $\ell = 1, \dots, 4$

and  $\ell = 5$  the rate  $\alpha$  was different. Further investigation is needed to find the reason for this. Another difficulty is the dependence on time, i.e. the number of levels  $L$  and the number of sums  $m_\ell$  depend on  $t$ . At the beginning the variability is small, then it increases, and after the process of mixing salt and fresh water has stopped, the variance decreases again.

The number of random samples required at each level was estimated by calculating the decay of the variances and the computational cost for each level. These estimates depend on the minimisation function in the MLMC algorithm.

To achieve the efficiency of the MLMC approach presented in this work, it is essential that the complexity of the numerical solution of each random realisation is proportional to the number of grid vertices on the grid levels. This holds only under special choice the numerical solvers, and we applied the geometric multigrid method implemented in the ug4 software toolkit, cf. [37, 49]. Our numerical tests confirm the expected efficiency. The random realizations do not depend on each other and have been computed concurrently on different nodes of the supercomputer Shaheen II at the King Abdullah University of Science and Technology.

In the numerical experiments, we computed the expected value and variance of the mass fraction in the whole domain and the solution at a few preselected points  $(t, \mathbf{x})$ . It turns out that the grid hierarchy of only 2 to 3 levels is sufficient for some QoIs. Note that a different type of porosity in (20) may lead to a different conclusion.

Our numerical results confirm that the MLMC is principally more numerically efficient than the MC method. Thus, sampling at different mesh levels helps to reduce the overall computational cost.

**Constraints.** 1. The time dependence is challenging. The optimal number of samples depends on the time moment  $t$ , and the spatial location  $\mathbf{x}$ , and may be small for some points and large for others. 2. Each new QoI requires new estimates of all parameters  $\alpha, \beta, \gamma$ , and the resulting MLMC performance graphics can be different.

**Future work.** A more realistic modeling of the fracture, porosity and permeability with more random variables can be considered.

**Acknowledgments.** For computing time, this research used Shaheen II, which is managed by the Supercomputing Core Laboratory at the King Abdullah University of Science and Technology (KAUST) in Thuwal, Saudi Arabia. We thank the KAUST HPC support team for their assistance with Shaheen II. This work was supported by the Alexander von Humboldt foundation.

## References

- [1] Angot P, Boyer F, Hubert F (2009) Asymptotic and numerical modelling of flow in fractured porous media. ESAIM: M2AN Mathematical Modelling and Numerical Analysis 43:239–275
- [2] Barrett R, Berry M, Chan TF, et al (1994) Templates for the Solution of Linear Systems: Building Blocks for Iterative Methods. Society for Industrial and Applied Mathematics, <https://doi.org/10.1137/1.9781611971538>

- [3] Bastian P, Birken K, Johannsen K, et al (2000) Parallel solution of partial differential equations with adaptive multigrid methods on unstructured grids. In: Jäger W, Krause E (eds) High performance computing in science and engineering. Springer, Berlin, pp 506–519
- [4] Bastian P, Chen Z, Ewing RE, et al (2000) Numerical simulation of multiphase flow in fractured porous media. In: Chen Z, et al. (eds) Numerical treatment of multiphase flows in porous media. Proceedings of the international workshop, Beijing, China, August 2–6, 1999., Lect. Notes Phys., vol 552. Springer, Berlin, pp 50–68
- [5] Blatman G, Sudret B (2010) An adaptive algorithm to build up sparse polynomial chaos expansions for stochastic finite element analysis. Probabilistic Engineering Mechanics 25(2):183 – 197. <https://doi.org/http://dx.doi.org/10.1016/j.probengmech.2009.10.003>
- [6] Bode F, Ferré T, Zigelli N, et al (2018) Reconnecting stochastic methods with hydrogeological applications: A utilitarian uncertainty analysis and risk assessment approach for the design of optimal monitoring networks. Water Resources Research 54(3):2270–2287. <https://doi.org/https://doi.org/10.1002/2017WR020919>
- [7] Carrera J (1993) An overview of uncertainties in modelling groundwater solute transport. Journal of Contaminant Hydrology 13(1):23 – 48. [https://doi.org/https://doi.org/10.1016/0169-7722\(93\)90049-X](https://doi.org/https://doi.org/10.1016/0169-7722(93)90049-X), chemistry and Migration of Actinides and Fission Products
- [8] Charrier J, Scheichl R, Teckentrup AL (2013) Finite element error analysis of elliptic pdes with random coefficients and its application to multilevel monte carlo methods. SIAM Journal on Numerical Analysis 51(1):322–352. <https://doi.org/10.1137/110853054>
- [9] Cliffe K, Giles M, Scheichl R, et al (2011) Multilevel monte carlo methods and applications to elliptic pdes with random coefficients. Computing and Visualization in Science 14(3):3–15. <https://doi.org/10.1007/s00791-011-0160-x>
- [10] Collier N, Haji-Ali AL, Nobile F, et al (2015) A continuation multilevel monte carlo algorithm. BIT Numerical Mathematics 55(2):399–432
- [11] Costa A (2006) Permeability-porosity relationship: A reexamination of the kozeny-carman equation based on a fractal pore-space geometry assumption. Geophysical Research Letters 33(2). <https://doi.org/10.1029/2005GL025134>
- [12] Cremer C, , Graf T (2015) Generation of dense plume fingers in saturated–unsaturated homogeneous porous media. Journal of Contaminant Hydrology 173:69 – 82. <https://doi.org/https://doi.org/10.1016/j.jconhyd.2014.11.008>

- [13] D'Angelo C, Scotti A (2012) A mixed finite element method for darcy flow in fractured porous media with non-matching grids. *ESAIM: Mathematical Modelling and Numerical Analysis* 46(02):465–489. <https://doi.org/10.1051/m2an/2011148>
- [14] Dhal L, Swain S (2022) Understanding and modeling the process of seawater intrusion: a review, pp 269–290. <https://doi.org/10.1016/B978-0-12-823830-1.00009-2>
- [15] Frolkovič P, De Schepper H (2001) Numerical modelling of convection dominated transport coupled with density driven flow in porous media. *Advances in Water Resources* 24(1):63–72. [https://doi.org/10.1016/S0309-1708\(00\)00025-7](https://doi.org/10.1016/S0309-1708(00)00025-7)
- [16] Fumagalli A, Scotti A (2013) A numerical method for two-phase flow in fractured porous media with non-matching grids. *Advances in Water Resources* 62:454–464. <https://doi.org/10.1016/j.advwatres.2013.04.001>, computational Methods in Geologic CO2 Sequestration
- [17] Giles MB (2008) Multilevel Monte Carlo path simulation. *Operations Research* 56(3):607–617
- [18] Giles MB (2015) Multilevel Monte Carlo methods. *Acta Numerica* 24:259–328
- [19] Graf T, Therrien R (2007) Variable-density Groundwater Flow and Solute Transport in Irregular 2D Fracture Networks. *Adv Water Resour* 30:455–468
- [20] Grillo A, Logashenko D, Stichel S, et al (2010) Simulation of density-driven flow in fractured porous media. *Advances in Water Resources* 33(12):1494–1507. <https://doi.org/10.1016/j.advwatres.2010.08.004>
- [21] Grillo A, Lampe M, Logashenko D, et al (2012) Simulation of salinity- and thermohaline-driven flow in fractured porous media. *Journal of Porous Media* 15(5):439–458. <https://doi.org/10.1615/JPorMedia.v15.i5.40>
- [22] Hackbusch W (1985) *Multi-Grid Methods and Applications*. Springer, Berlin
- [23] Hackbusch W (1994) *Iterative Solution of Large Sparse Systems of Equations*. Springer, New-York
- [24] Haji-Ali AL, Nobile F, von Schwerin E, et al (2016) Optimization of mesh hierarchies in multilevel Monte Carlo samplers. *Stoch Partial Differ Equ Anal Comput* 4(1):76–112. <https://doi.org/10.1007/s40072-015-0049-7>
- [25] Henry HR (1964) Effects of dispersion on salt encroachment in coastal aquifers, in 'seawater in coastal aquifers'. US Geological Survey, Water Supply Paper 1613:C70–C80
- [26] Hoel H, Von Schwerin E, Szepessy A, et al (2012) Adaptive multilevel Monte Carlo simulation. In: *Numerical Analysis of Multiscale Computations*. Springer,

- [27] Hoel H, von Schwerin E, Szepessy A, et al (2014) Monte Carlo Methods and Applications 20(1):1–41. <https://doi.org/doi:10.1515/mcma-2013-0014>
- [28] Hoteit H, Firoozabadi A (2008) An efficient numerical model for incompressible two-phase flow in fractured media. Advances in Water Resources 31(6):891–905. <https://doi.org/10.1016/j.advwatres.2008.02.004>
- [29] Khoromskij BN, Litvinenko A, Matthies H (2009) Application of hierarchical matrices for computing the Karhunen-Loève expansion. Computing 84(1-2):49–67. <https://doi.org/10.1007/s00607-008-0018-3>
- [30] Litvinenko A, Yucel AC, Bagci H, et al (2019) Computation of electromagnetic fields scattered from objects with uncertain shapes using multilevel monte carlo method. IEEE Journal on Multiscale and Multiphysics Computational Techniques 4:37–50. <https://doi.org/10.1109/JMMCT.2019.2897490>
- [31] Logashenko D, Litvinenko A, Tempone R, et al (2024) Uncertainty quantification in the henry problem using the multilevel monte carlo method. Journal of Computational Physics 503:112854. <https://doi.org/https://doi.org/10.1016/j.jcp.2024.112854>
- [32] Martin V, Jaffré J, Roberts JE (2005) Modeling fractures and barriers as interfaces for flow in porous media modeling fractures and barriers as interfaces for flow in porous media. SIAM J Sci Comput 26(5):1667–1691. <https://doi.org/10.1137/S1064827503429363>
- [33] Martinez-Landa L, Carrera J (2006) A methodology to interpret cross-hole tests in a granite block. Journal of Hydrogeology 325(1-4):222–240
- [34] Panda M, Lake W (1994) Estimation of single-phase permeability from parameters of particle-size distribution. AAPG Bull 78:1028–1039
- [35] Pape H, Clauser C, Iffland J (1999) Permeability prediction based on fractal pore-space geometry. Geophysics 64(5):1447–1460. <https://doi.org/10.1190/1.1444649>
- [36] Reiter S, Logashenko D, Grillo A, et al (2012) Preparation of grids for simulations of groundwater flow in fractured porous media. Computing and Visualization in Science 15:209–225. <https://doi.org/10.1007/s00791-013-0210-7>
- [37] Reiter S, Vogel A, Heppner I, et al (2013) A massively parallel geometric multigrid solver on hierarchically distributed grids. Computing and Visualization in Science 16(4):151–164. <https://doi.org/10.1007/s00791-014-0231-x>

- [38] Reiter S, Logashenko D, Stichel S, et al (2014) Models and simulations of variable-density flow in fractured porous media. *International Journal of Computational Science and Engineering* 9(5-6):416–432. <https://doi.org/10.1504/IJCSE.2014.064527>
- [39] Riva M, Guadagnini A, Dell’Oca A (2015) Probabilistic assessment of seawater intrusion under multiple sources of uncertainty. *Advances in Water Resources* 75(C):93–104. <https://doi.org/10.1016/j.advwatres.2014.11.002>
- [40] Rubin Y (2003) *Applied Stochastic Hydrogeology*. Oxford University Press, <https://doi.org/10.1093/oso/9780195138047.001.0001>
- [41] Shikaze SG, Sudicky EA, Schwartz FW (1998) Density-dependent solute transport in discretely-fractured geologic media: is prediction possible? *Journal of Contaminant Hydrogeology* 34:273–291
- [42] Simpson MJ, Clement T (2003) Theoretical Analysis of the worthiness of Henry and Elder problems as benchmarks of density-dependent groundwater flow models. *Adv Water Resour* 26:17–31
- [43] Simpson MJ, Clement TP (2004) Improving the worthiness of the Henry problem as a benchmark for density-dependent groundwater flow models. *Water Resources Research* 40(1):W01504. <https://doi.org/10.1029/2003WR002199>
- [44] Sorek S, Borisov V, Yakirevich A (2001) A two-dimensional Areal Model for Density Dependent Flow Regime. *Transport in Porous Media* 43:87–105
- [45] Sudret B (2008) Global sensitivity analysis using polynomial chaos expansions. *Reliability engineering & system safety* 93(7):964–979
- [46] Tartakovsky D (2013) Assessment and management of risk in subsurface hydrology: A review and perspective. *Advances in Water Resources* 51:247 – 260. <https://doi.org/https://doi.org/10.1016/j.advwatres.2012.04.007>, 35th Year Anniversary Issue
- [47] Teckentrup A, Scheichl R, Giles M, et al (2013) Further analysis of multi-level monte carlo methods for elliptic pdes with random coefficients. *Numerische Mathematik* 125(3):569–600
- [48] Vereecken H, Schnepf A, Hopmans J, et al (2016) Modeling soil processes: Review, key challenges, and new perspectives. *Vadose Zone Journal* 15(5):vzj2015.09.0131. <https://doi.org/https://doi.org/10.2136/vzj2015.09.0131>
- [49] Vogel A, Reiter S, Rupp M, et al (2013) Ug 4: A novel flexible software system for simulating pde based models on high performance computers. *Computing and Visualization in Science* 16(4):165–179. <https://doi.org/10.1007/s00791-014-0232-9>



- [50] Voss C, Souza W (1987) Variable density flow and solute transport simulation of regional aquifers containing a narrow freshwater-saltwater transition zone. *Water Resources Research* 23(10):1851–1866. <https://doi.org/10.1029/WR023i010p01851>